CHEMISTRY OF MATERIALS

Article

pubs.acs.org/cm

Combinational Synthetic Approaches for Isoreticular and Polymorphic Metal–Organic Frameworks with Tuned Pore Geometries and Surface Properties

Seok Jeong,[†] Dongwook Kim,[†] Sunyoung Shin,[†] Dohyun Moon,[‡] Sung June Cho,[§] and Myoung Soo Lah*,[†]

[†]Department of Chemistry, Ulsan National Institute of Science & Technology, Ulsan 689-805, Korea

[‡]Pohang Accelerator Laboratory, Pohang 790-784, Korea

[§]Department of Applied Chemical Engineering and the Research Institute for Catalysis, Chonnam National University, Gwangju 500-757, Korea

Supporting Information

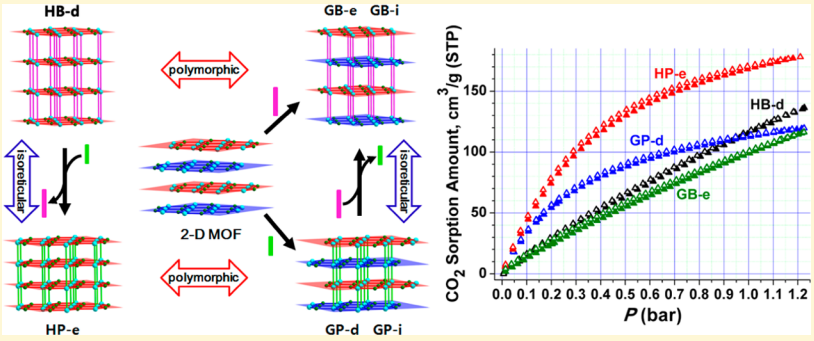

ABSTRACT: Isoreticular and polymorphic 3-D MOFs were prepared via the combination of direct solvothermal reactions, postsynthetic ligand exchanges of the MOFs prepared via the direct solvothermal reactions, and postsynthetic ligand insertions into a 2-D MOF. The appropriate pore dimensions, surface areas, and adsorption enthalpies of the MOFs combined well to produce the largest working CO_2 capture capacities via the pressure swing adsorption process.

INTRODUCTION

Porous metal–organic frameworks (MOFs) are very interesting materials because of their large surface areas and the tunability of the surface properties.[1] The pore geometries and surface properties of the MOFs can be utilized in various applications, including gas storage and separation.[2]

The conventional approach for the preparation of MOFs is a one-pot solvothermal reaction with appropriate building blocks. However, the tuning of the pore geometry with desired surface property via a direct one-pot solvothermal reaction is a challenging task. Postsynthetic modification of MOFs is an alternative approach to obtaining MOFs with a tuned pore property.[3] Postsynthetic covalent modification of the organic linker of the MOF or postsynthetic dative modification on the framework metal center can be utilized for the modulation of pore geometry and surface property. Postsynthetic exchanges of the framework metal ions[4] and the organic ligands[5] in MOFs have also been reported as new approaches for the tuning of pore properties.

Recent investigations on MOFs are focused on CO_2 captures rather than CO_2 storages.[6] Potential industrial postcombustion CO_2 capture processes require various pore characteristics of the MOFs, depending on the specific process conditions.[7] The presence of a strong adsorption site in the MOF is very important for CO_2 capture in vacuum swing adsorption (VSA) and temperature swing adsorption (TSA) processes of real flue gases with typical ~15% CO_2 fraction.[8] The large adsorption enthalpy of the MOFs with strong adsorption sites such as open metal sites[9] and amine functional groups[10] is one of the most important factors determining the working CO_2 capture capacities in these processes. However, for the pressure swing adsorption (PSA) process between the pressurized real flue gas of ~6 bar and the depressurized gas of ~1 bar, a moderate adsorption enthalpy of MOFs with tuned pore geometry and surface property is more important in determining the working CO_2 capture capacities than a large surface area and/or large adsorption enthalpy.[7]

Here, we report the preparation and characterization of a series of isoreticular and polymorphic MOFs with tuned pore geometries and surface properties via combinational synthetic approaches, direct one-pot solvothermal reaction, and subsequent postsynthetic ligand exchange (PLE) and postsynthetic

Received: December 30, 2013
Revised: January 23, 2014
Published: January 24, 2014

   dx.doi.org/10.1021/cm404239s | Chem. Mater. 2014, 26, 1711–1719

ligand insertion (PLI) of the MOF prepared via the direct one-pot solvothermal reaction. The pore properties, including the pore dimensions and geometries and the specific surface areas of a series of MOFs prepared via the combinational synthetic approaches, were investigated. The potentials of the MOFs as postcombustion CO_2 capture materials based on the working CO_2 capture capacities in VSA and PSA processes are discussed.

EXPERIMENTAL SECTION

General Procedures. All reagents were purchased from commercial sources and used without further purification. Elemental analysis (EA) (C, H, and N) was performed at the Central Research Facilities of the Ulsan National Institute of Science & Technology (Ulsan, Korea). Fourier transform infrared (FT-IR) spectra were recorded as KBr pellets with a NICOLET iS 10 FT-IR spectrophotometer (4000−400 cm^{-1}). Nuclear magnetic resonance (NMR) spectra were obtained on a Varian-600 NMR spectrometer. Thermal gravimetric analysis (TGA) data were recorded using a TA Instruments Q-600 series thermal gravimetric analyzer under flowing nitrogen gas. Powder X-ray diffraction (PXRD) data were recorded using a Bruker D2 Phaser automated diffractometer at room temperature, with a step size of $2\theta = 0.02°$. Simulated PXRD patterns were calculated using the Material Studio software package[11] employing a structural model from single-crystal data.

Preparation of MOFs via Direct Solvothermal Reaction. *[Ni(HBTC)(DMF)$_2$] and HB-d.* [Ni(HBTC)$(DMF)_2$] (where H_3BTC = 1,3,5-benzenetricarboxylic acid) and HB-d (HB-d: [Ni(HBTC)-(bipy)] of an **hms** topology with 4,4′-bipyridine (**b**ipy) pillar prepared via **d**irect solvothermal reaction)[12] were prepared in DMF according to the reported procedure.[13] The crystals of [Ni(HBTC)$(DMF)_2$] and HB-d were harvested and washed using *N*,*N*′-dimethylformamide (DMF) and then air-dried at ambient temperature for a couple of hours. The activated sample was prepared by soaking the crystals of HB-d in fresh DMF for 2−3 d and in methylene chloride for 1 d and then vacuum-drying at ambient temperature overnight.

GP-d (GP-d: [Ni(HBTC)(pz)] of a **gra** topology with pyrazine (**p**z) pillar prepared via **d**irect solvothermal reaction) was prepared using a procedure that was slightly modified from the reported procedure.[14] A mixture of $Ni(NO_3)_2{\cdot}6H_2O$ (0.0955 g, 0.328 mmol), H_3BTC (0.0583 g, 0.277 mmol), and pz (0.0660 g, 0.824 mmol) was dissolved in 10 mL of DMF. The solution in a tightly sealed 20 mL vial was heated at 70 °C for 2 d to form greenish cyan crystals. The crystals harvested were washed using fresh DMF and then air-dried in ambient conditions for an hour. Yield = 0.087 g. The activated sample was prepared by soaking the crystals of GP-d in fresh DMF for 2−3 days and in methylene chloride for 1 d and then vacuum-drying at 50 °C for 2 d. The elemental analysis (EA) was performed using the activated sample exposed in air for a couple of minutes before the analysis. Elem. Anal calcd for [Ni(HBTC)(pz)]·$1.6H_2O$ ($C_{13}H_{11.2}N_2O_{7.6}Ni$, fw = 375.73 g/mol). Found. (Calcd): C = 41.63 (41.56) %; H = 3.01 (3.00) %; N = 7.45 (7.46) %. IR of the activated sample (KBr, cm^{-1}): 3379 (vs, b), 3123 (w, b), 2928 (vw, b), 1881 (w, b), 1707 (s, sh), 1658 (vs), 1612 (vs), 1544 (s), 1441 (vs), 1421 (s, sh), 1373 (vs), 1261 (m, b), 1233 (w, sh), 1188 (vw), 1162 (m), 1125 (m), 1096 (m), 1065 (m), 1022 (w), 937 (w), 904 (w), 866 (w), 815 (m), 797 (w, sh), 760 (m), 745 (m), 719 (m), 667 (w), 543 (m, b), 520 (w, sh), 481 (m), 453 (w), 417 (w).

Preparation of MOFs via Postsynthetic Ligand Exchange (PLE). Before the ligand exchange and the ligand insertion, the as-synthesized single crystals were presoaked in DMF for a couple of days to remove any remaining reactants and side products present in the solvent cavities. After decanting the solvent, the crystals were air-dried at ambient temperature for a couple of hours.

HP-e (HP-e: [Ni(HBTC)(pz)] of an **hms** topology with **p**z pillar prepared via PL**E** reaction) was prespared as follows. A 100−200 mg amount of the crystals of HB-d presoaked in DMF was transferred to a vial of 40 mL of 1.0 M pz DMF solution, and the solution in the vial was stored in an oven at 100 °C for 1−2 weeks depending on the sample amount. The solution was refreshed 4−7 times during the soaking. The progress of the ligand exchange was checked using PXRD. When the ligand exchange was completed, the harvested crystals were washed using fresh DMF more than five times and then air-dried at ambient temperature for 1 h. IR of HP-e (KBr, cm^{-1}): 3396 (vs, b), 3124 (w, b), 3087 (w, b), 3065 (w, b), 2934 (w, b), 1698 (s, b), 1667 (m, sh), 1660 (m), 1616 (s), 1557 (s, sh), 1538 (s), 1453 (m, sh), 1436 (s), 1422 (s), 1402 (m), 1376 (vs), 1322 (w, b), 1276 (m, b), 1238 (m, sh), 1189 (vw), 1162 (w), 1125 (w), 1109 (vw), 1091 (w), 1065 (m), 832 (vw), 811 (w), 767 (w, sh), 751 (s), 732 (m), 722 (w, sh), 685 (w), 661 (vw), 609 (vw), 548 (vw), 516 (vw), 482 (m), 417 (vw). The activated sample was prepared by soaking the crystals of HP-e in fresh DMF for 2−3 d and in methylene chloride for 1 d and then vacuum-drying at ambient temperature for 3 d. EA was performed on the activated sample reexposed in air for a couple of minutes before the analysis. Elem. Anal calcd for [Ni(HBTC)(pz)]·$1.2H_2O$ ($C_{13}H_{10.4}N_2O_{7.2}Ni$, fw = 368.53 g/mol). Found (Calcd): C = 42.67 (42.37) %; H = 2.92 (2.84) %; N = 7.52 (7.60) %. IR of the activated sample (KBr, cm^{-1}): 3396 (vs, b), 3126 (w, b), 3082 (w, b), 2932 (w, b), 1705 (m, sh), 1664 (vs), 1613 (vs), 1541 (s), 1444 (vs), 1422 (s), 1379 (vs), 1261 (m, b), 1184 (w, sh), 1163 (m), 1124 (m), 1095 (m), 1065 (m), 1022 (w), 936 (vw), 914 (w), 858 (vw), 816 (m), 797 (vw, sh), 760 (w, sh), 747 (m), 720 (m), 689 (w, sh), 669 (vw), 544 (w), 522 (w, sh), 483 (m), 455 (vw, sh), 418 (w).

GB-e (GB-e: [Ni(HBTC)(bipy)] of a **gra** topology with **b**ipy pillar prepared via PL**E** reaction) was prepared as follows. Approximately 200 mg of the crystals of GP-d presoaked in DMF was transferred to a vial of 20 mL of 0.2 M bipy DMF solution, and the solution in the vial was stored in an oven at 70 °C for 4 d. When the ligand exchange was completed, the harvested crystals were washed using fresh DMF more than five times and then air-dried at ambient temperature for an hour. Single crystals good enough for structure analysis were obtained by soaking approximately 100 mg of the crystals of GP-d presoaked in DMF in a capped vial of a 10 mL amount of 0.1 M bipy DMF solution at ambient temperature for three months. The activated sample was prepared by soaking the crystals of GB-e in fresh DMF for 2−3 d and in methylene chloride for 2 d. During the soaking in methylene chloride, the solvent was refreshed more than seven times, and then the sample was vacuum-dried at ambient temperature for 2 d. EA was performed on the activated sample reexposed to air for a couple of minutes before the analysis. Elem. Anal calcd for [Ni(HBTC)(bipy)]·$3.3H_2O$ ($C_{19}H_{18.6}N_2O_{9.3}Ni$, fw = 482.46 g/mol). Found (Calcd): C = 47.23 (47.30) %; H = 3.84 (3.89) %; N = 5.75 (5.81) %. IR of the activated sample (KBr, cm^{-1}): 3357 (vs, b), 3238 (vs, b), 3101 (s, b), 1953 (vw, b), 1872 (vw, b), 1700 (m), 1656 (m), 1611 (vs), 1550 (vs), 1492 (w), 1433 (m), 1417 (m), 1365 (vs), 1320 (w, sh), 1262 (m), 1221 (m), 1188 (w), 1103 (w), 1069 (w), 1047 (vw), 1011 (w), 933 (w), 900 (vw, sh), 857 (w), 814 (m), 764 (m), 717 (s), 684 (m, sh), 636 (m), 574 (w), 542 (vw, b), 518 (vw, b), 460 (vw), 416 (vw).

Preparation of MOFs via Postsynthetic Ligand Insertion (PLI). GP-i (GP-i: [Ni(HBTC)(pz)] of a **gra** topology with **p**z pillar prepared via PL**I** reaction) could be prepared via postsynthetic pz insertion into 2-D [Ni(HBTC)$(DMF)_2$] in DMF. Approximately 200 mg of the crystals of [Ni(HBTC)$(DMF)_2$] was transferred to a vial of 20 mL of 0.5 M pz DMF solution, and the solution in the tightly sealed vial was stored in an oven at 100 °C for 11 d. The progress of the ligand insertion was checked using PXRD. When the ligand insertion was completed, the harvested crystals were washed using fresh DMF more than 3−4 times and then air-dried at ambient temperature for 1 h. The crystals presoaked in DMF were soaked in methylene chloride for 2 d, and the solvent was refreshed five times during the soaking. The complete replacement of the solvent DMF by methylene chloride was checked using ^1H NMR spectroscopy.

GB-i (GB-i: [Ni(HBTC)(bipy)] of a **gra** topology with **b**ipy pillar prepared via PL**I** reaction) could be prepared via postsynthetic bipy insertion into 2-D [Ni(HBTC)$(DMF)_2$] in DMF. Approximately 200 mg of the crystals of [Ni(HBTC)$(DMF)_2$] was transferred to a vial of 20 mL of 0.5 M bipy DMF solution, and the solution in the tightly sealed vial was stored in an oven at 100 °C for 11 d. The progress of the ligand insertion was checked using PXRD. When the ligand

dx.doi.org/10.1021/cm404239s | *Chem. Mater.* 2014, 26, 1711−1719

insertion was completed, the harvested crystals were washed using fresh DMF more than 3−4 times and then air-dried at ambient temperature for an hour. The crystals presoaked in DMF were soaked in methylene chloride for 2 d, and the solvent was refreshed five times during the soaking. The complete replacement of the solvent DMF by methylene chloride was checked using ^{1}H NMR spectroscopy. The activated sample was prepared by vacuum-drying GB-i at ambient temperature for 2 d. Elem. Anal calcd for [Ni(HBTC)(bipy)]·1.9H_2O ($C_{19}H_{15.8}N_2O_{7.9}Ni$, fw = 456.23 g/mol). Found (Calcd): C = 49.91 (49.91) %; H = 3.45 (3.48) %; N = 6.25 (6.13) %.

Gas Sorption Measurements. All the gas sorption isotherms were measured using a BELSORP-max (BEL Japan, Inc.) and an ASAP 2020 (Micromeritics Instrument Corporation) absorption system employing a standard volumetric technique up to saturated pressure. The N_2 (purity = 99.9999%) sorption isotherms were monitored at 77 K. The adsorption data in the pressure range <0.1 P/P_0 were fitted to the Brunauer−Emmett−Teller (BET) equation to determine the BET specific surface area. The entire set of adsorption data was used to obtain the Langmuir specific surface area. The CO_2 (purity = 99.999%) sorption isotherms were monitored at 195, 273, and 298 K.

RESULT AND DISCUSSION

Direct Solvothermal Reaction. HB-d could be obtained via direct solvothermal reaction of Ni(II) ion with H_3BTC in the presence of bipy as a pillaring linker.[13] However, the attempt to reproduce the isoreticular MOF, HP-d ([Ni(HBTC)(pz)] of an **hms** topology with **p**z pillar prepared via **d**irect solvothermal reaction), using the reported solvothermal synthetic procedure[14] with Ni(II), H_3BTC, and pz in 1:1:1 mol ratio produced a mixture of [Ni(HBTC)$(DMF)_2$] and GP-d (Figure 1).

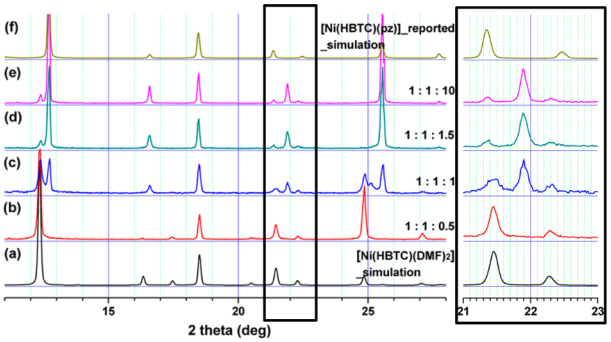

Figure 1. PXRD patterns of the samples prepared according to the reported synthetic procedure for [Ni(HBTC)(pz)] of $Ni(NO_3)_2$·$6H_2O$, H_3BTC, and pz in 1:1:1 mole ratio and other mole ratios.

While the reaction in a 1:1:0.5 mole ratio only produced [Ni(HBTC)$(DMF)_2$] (Figure 1b), the similar reaction in a 1:1:1.5 mole ratio or in higher pz mole ratio resulted in GP-d as a pure phase (Figure 1d,e). The PXRD pattern of GP-d is similar to that of HP-d reported as the **hms** topology but not identical (Figure 1f).[15]

PLE. HP-e could be obtained by soaking HB-d in pz DMF solution (Supporting Information Figure S1). The PXRD pattern of HP-e is very similar to that of GP-d but is not identical (Figure 2). The single-crystal structure analyses of GP-d and HP-e revealed that they are polymorphic MOFs of the same [Ni(HBTC)(pz)] formula with the same 3,5-connection but different net topologies, **gra** and **hms** topologies, respectively (Figure 3 and Supporting Information Figure S2).[16]

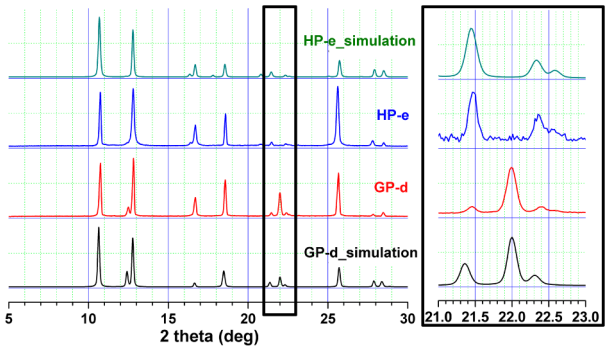

Figure 2. PXRD patterns of GP-d and of HP-e and their simulated PXRD patterns from the corresponding single-crystal structure models.

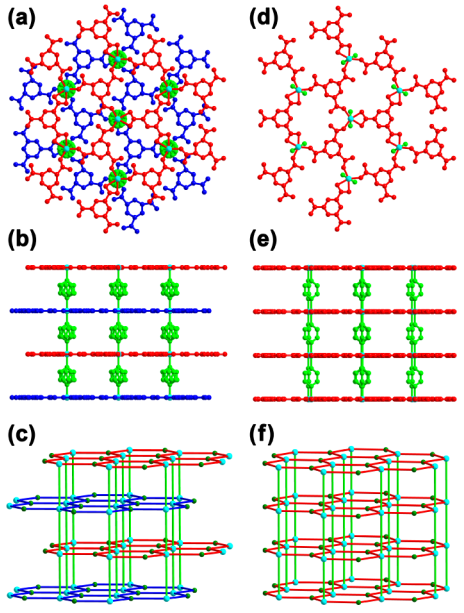

Figure 3. Ball-and-stick diagrams of GP-d and HP-e. (a) Top and (b) side views of the ball-and-stick diagram of GP-d. (c) A schematic drawing of GP-d that shows a **gra** topology. (d) Top and (e) side views of the ball-and-stick diagram of HP-e. (f) A schematic drawing of HP-e that shows a **hms** topology. In (c) and (f), the 5-c metal ion is shown as a cyan ball, and the 3-c $HBTC^{2-}$ ligand is shown as a green ball.

In GP-d, the Ni(II) ions in the 2-D sheet, [Ni(HBTC)], of an **hcb** topology are interconnected to the Ni(II) ions of the next neighboring 2-D sheets via pillaring pz linkers to form the 3,5-c network of a **gra** topology (Figure 3a−c). The framework of the **gra** topology generates the cage-like pores (Figure 4 and Supporting Information Figure S3) interconnected to form a three-dimensional microporous structure with the total pore volume consisting of 41.3% of the total unit cell volume. In HP-e, the Ni(II) ions in the 2-D sheet are also interconnected to the Ni(II) ions of the next neighboring 2-D sheets via pillaring pz linkers, as in GP-d. However, the 2-D sheets in HP-e are stacked to form the framework of a 3,5-c **hms** topology (Figure 3d−f). The polymorphic framework of the **hms** topology produces a different kind of the cage-like pores being aligned along the crystallographic *c*-axis to form a 1-D channel. The channels are interconnected along the crystallographic *ab*-plane to form a 3-D microporous structure with the pore volume

dx.doi.org/10.1021/cm404239s | *Chem. Mater.* 2014, 26, 1711−1719

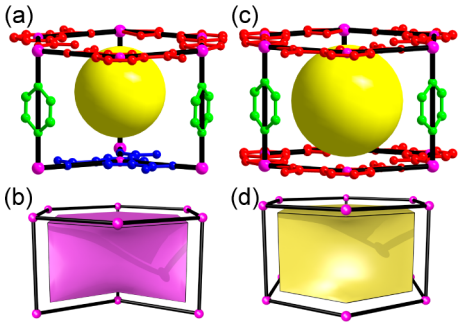

Figure 4. (a) Ball-and-stick model of the cage-like pore of GP-d of a **gra** topology with a yellow dummy ball in the center of the cavity and (b) the corresponding tile with the net. (c) Ball-and-stick model of the cage-like pore of HP-e of an **hms** topology with a yellow dummy ball in the center of the cavity and (d) the corresponding tile with the net.

consisting of 46.9% of the total unit cell volume, which is slightly larger than the pore volume of GP-d.

While the direct solvothermal reaction of Ni(II) with H_3BTC in the presence of bipy only produced HB-d, GB-e could be obtained via postsynthetic ligand exchange. The PXRD patterns of HB-d and GB-e are slightly different from each other (Figure 5). While a peak at ~11.5° was observed in GB-e, there is no

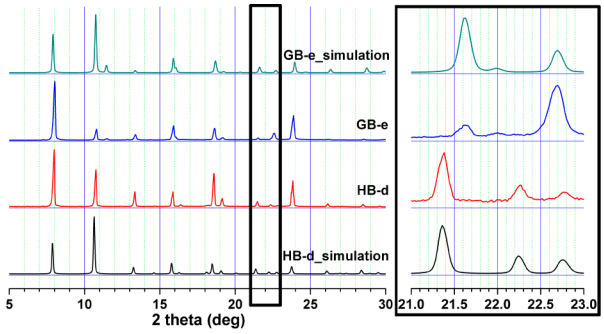

Figure 5. PXRD patterns of HB-d and GB-e.

corresponding peak in HB-d. While there is a peak at ~22.3° in HB-d, no corresponding peak is observed in GB-e. The two peaks observed at ~21.4° and ~22.8° in HB-d were shifted to ~21.6° and ~22.7°, respectively, in GB-e. In addition, the crystal color of the activated GB-e is also slightly different from that of the activated HB-d (Supporting Information Figure S2).

The single-crystal structure analysis confirmed that GB-e and HB-d are also polymorphic MOFs of the same 3,5-connection but different net topologies, **gra** and **hms** topologies, respectively (Figure 6 and Supporting Information Figures S4–S5). GB-e of the longer bipy has a larger solvent cavity (47.9% of the total unit cell) than that of GP-d of the same net topology, **gra**, but of the shorter pz (41.3% of the total unit cell volume). On the other hand, the solvent cavity volume of GB-e of the **gra** topology is smaller than that of HB-d of the same bipy pillar but of different net topology, **hms** (54.8% of the total unit cell volume).[13]

PLI. GP-i could also be obtained via the insertion of pz into the 2-D MOF of an **hcb** topology. In the reported 2-D MOF [Ni(HBTC)$(DMF)_2$], the 2-D sheets with both Ni(II) ion and $HBTC^{2-}$ as 3-c nodes are stacked in a staggered fashion to form $-(AB)_n-$ layered structure as the graphene sheets in a hexagonal graphite structure (Figure 7a–c).

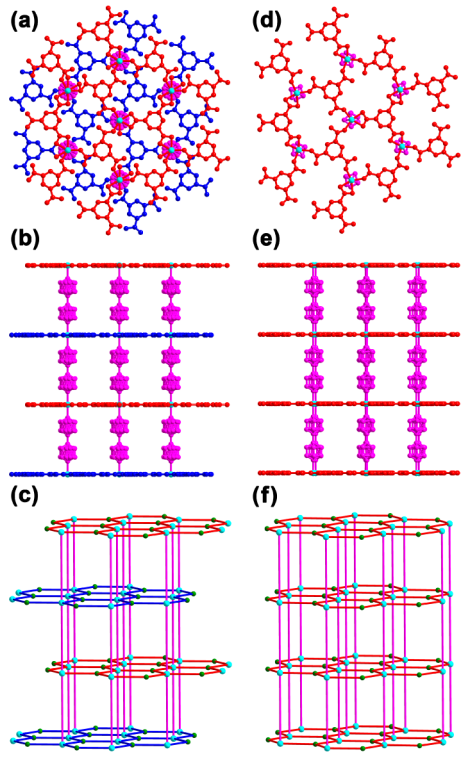

Figure 6. Ball-and-stick diagrams of GB-e of a **gra** net topology and HB-d of an **hms** net topology. (a) Top and (b) side views of the ball-and-stick diagram of GB-e. (c) The schematic drawing of GB-e that shows a 3,5-conneted **gra** net topology. (d) Top and (e) side views of the ball-and-stick diagram of HB-d. (f) A schematic drawing of HB-d that shows a 3,5-conneted **hms** net topology. In (c) and (f), the 5-c metal ion is a cyan ball and the 3-c $HBTC^{2-}$ ligand is a green ball.

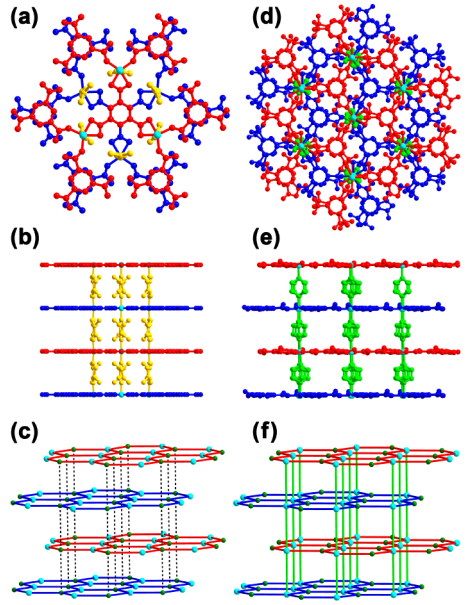

Figure 7. Ball-and-stick diagrams of (a–c) the 2-D MOF, [Ni(HBTC)$(DMF)_2$], of an **hcb** topology and (d–f) the 3-D MOF, GP-i of a **gra** topology.

However, the alternating $-(AB)_n-$ staggered stacking of the 2-D sheets is different from that of the 2-D sheets in the 3-D MOFs of the **gra** topology. While the Ni(II) ions in all of the sheets at the 3-D MOFs of the **gra** topology are aligned along

dx.doi.org/10.1021/cm404239s | *Chem. Mater.* 2014, 26, 1711–1719

the crystallographic *c*-axis (Figure 7d–f), the $HBTC^{2-}$ ligands in all of the sheets of 2-D $[Ni(HBTC)(DMF)_2]$ are aligned along the crystallographic *c*-axis (Figure 7a–c). For the construction of a 3-D MOF via the insertion of a pillaring ligand, two different types of structural reorganization of the 2-D sheets are possible. The first type of structural reorganization is the rotation of the 2-D sheets to align the Ni(II) ions along the crystallographic *c*-axis with the adjustment of the intersheet distance for the construction of an MOF of an **hms** topology, which is less likely to happen because of the extensive movement of the parts of the sheets away from the rotation axis. The other type of structural reorganization is a translational structural reorganization, which is a sliding of the sheets parallel to the crystallographic *ab*-plane to align the Ni(II) ions along the crystallographic *c*-axis with a marginal adjustment of the intersheet distance to accommodate the pillaring linker between the sheets, which could lead to the MOF of the **gra** topology. Soaking the crystals of the 2-D MOF in pz DMF solution resulted in the insertion of pz between the 2-D sheets to form crystalline product of GP-i. The PXRD pattern of the product is slightly different from that of HP-e of an **hms** topology but very similar to that of GP-d of a **gra** topology (Figure 8). The single crystal structure analysis confirms that GP-i is isostructural to GP-d.[17]

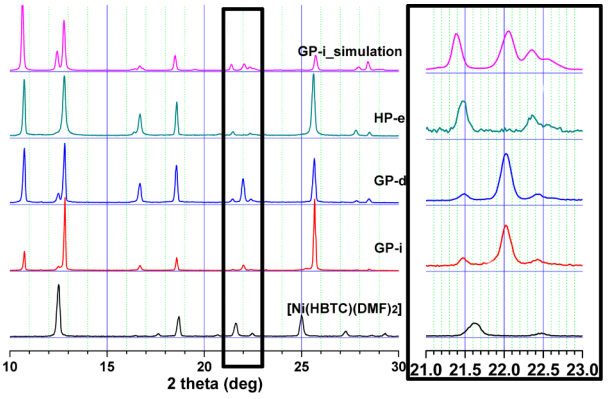

Figure 8. PXRD pattern of GP-i prepared via postsynthetic pz insertion into 2-D $[Ni(HBTC)(DMF)_2]$ and a comparison with those of GP-d and HP-e.

The postsynthetic insertion of bipy into the 2-D MOF also leads to GB-i, which is isostructural to GB-e obtained via the PLE reaction. The PXRD pattern of GB-i shows the same characteristic peaks observed in the PXRD pattern of GB-e (Figure 9), which tells us that the postsynthetically inserted MOF is the 3-D MOF, [Ni(HBTC)(bipy)], of the **gra** topology.

Isoreticular and Polymorphic MOFs via the Combinational Synthetic Approaches. Via the combinational synthetic approaches, either two sets of isoreticular MOFs, HB-d and HP-e of the same **hms** topology and GP-d (or GP-i) and GB-e (or GB-i) of the same **gra** topology, or two sets of polymorphic MOFs, HB-d and GB-e (or GB-i) of the same [Ni(II)(HBTC)(bipy)] formula and HP-e and GP-d (or GP-i) of the same [Ni(II)(HBTC)(pz)] formula, could be obtained (Scheme 1).

HB-d could be prepared via a direct one-pot solvothermal reaction using Ni(II) ion and $HBTC^{2-}$ as components for the 2-D sheet and using bipy as a pillaring component between the 2-D sheets. However, the similar one-pot solvothermal reaction

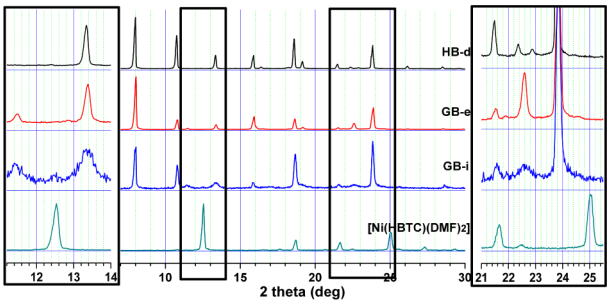

Figure 9. PXRD pattern of GB-i via postsynthetic bipy insertion into 2-D $[Ni(HBTC)(DMF)_2]$ and a comparison with those of HB-d and GB-e.

Scheme 1. Preparation of HB-d, GP-d, GB-e, HP-e, GB-i, and GP-i via the Combinational Synthetic Approaches

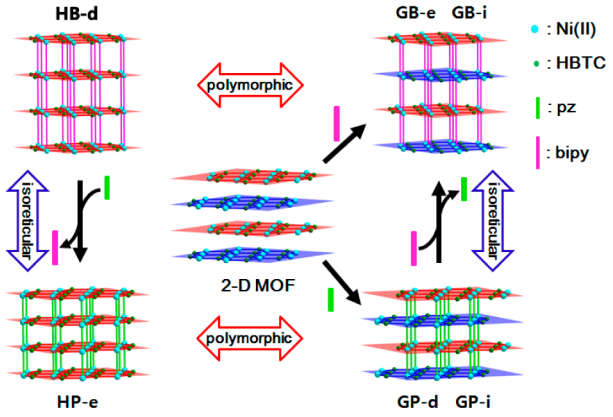

in the presence of pz as a pillaring component only produced GP-d rather than isoreticular HP-d. HP with the pz as a pillaring linker could only be obtained via the PLE of the bipy pillar of HB-d. HP-e obtained via the PLE is polymorphic to GP-d that is prepared via the direct solvothermal reaction. GB could be obtained either via the PLE of the pillaring pz linker of GP-d of the same **gra** topology or via the PLI of the pillaring pz linker into 2-D $[Ni(HBTC)(DMF)_2]$.

Gas Sorption Behaviors. *Activation of the MOFs.* The solvent molecules in the pores can be removed by soaking the MOFs in volatile methylene chloride and vacuuming at either ambient temperature or 50 °C. The proper activation of the samples was confirmed by using the ^1H NMR spectra, TGA data, and the PXRD studies of the activated samples (Supporting Information Figures S6–S10).

N_2 Adsorptions. The N_2 sorption studies on the activated polymorphic MOFs confirmed the microporosity of the frameworks expected from their single-crystal structures. Both adsorption isotherms of N_2 on HP-e and GP-d at 77 K are typical type I (Figure 10). The N_2 uptake amount on HP-e of an **hms** topology at $P/P_0 \approx 1$ is slightly larger than that on GP-d of a **gra** net topology (Table 1), which agrees well with the different solvent cavity volumes calculated based on the single-crystal structures of the two polymorphic frameworks of different net topologies. As expected from the weakly interacting property of N_2 with the pore surface of the MOFs, the adsorption amounts of N_2 on GP-d and HP-e at 293 K are negligible.

The N_2 adsorption isotherms of the other two activated polymorphic MOFs, HB-d and GB-e (or GB-i), at 77 K are also typical type I, which suggests that all of the MOFs are as

dx.doi.org/10.1021/cm404239s | *Chem. Mater.* 2014, 26, 1711–1719

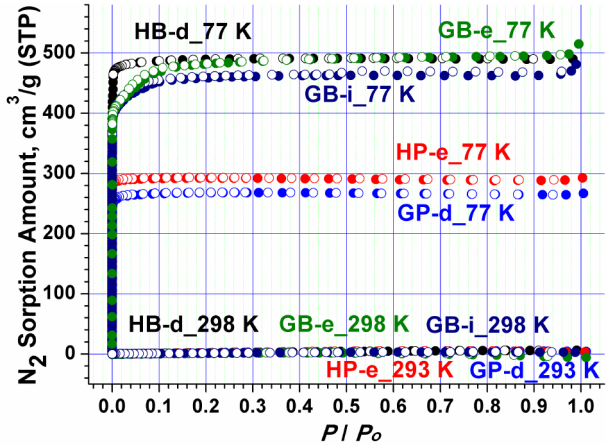

Figure 10. N_2 sorption isotherms on the activated HB-d, GP-d, HP-e, GB-e, and GB-i at 77 and 293 K (or 298 K).

Table 1. N_2 Sorption Behaviors and Pore Properties of the Activated MOFs, HB-d, GP-d, HP-e, GB-e, and GB-i

MOFs	N_2 uptake (cm^3/g), 77 K, ~1 bar	BET surface area (m^2/g)	Langmuir surface area (m^2/g)	$V_{p,measured}$ (cm^3/g)	$V_{p,calculated}$ (cm^3/g)	$d_{p,avg}$ (Å)
HB-d	490	1940	2130	0.76	0.72	10.2
GP-d	267	1090	1160	0.41	0.39	9.3
HP-e	293	1210	1270	0.45	0.45	9.1
GB-e	498	1840	2160	0.77	0.59	9.8
GB-i	465	1790	2010	0.74	–	8.8

microporous as GP-d and HP-e, even though the pore volumes of HB-d and GB-e (or GB-i) with the longer bipy pillar are larger than those of HP-e and GP-d with the shorter pz pillar. The N_2 uptake amount on GB-e (or GB-i) of a **gra** topology with the bipy pillar at $P/P_0 \approx 1$ is significantly larger than those on GP-d and HP-e with the shorter pz pillar and similar to that on HB-d with the same bipy pillar but of a different **hms** topology (Table 1).[18] The observed pore volume of GB-e (0.77 cm^3/g) is much larger than the calculated pore volume of GB-e (0.59 cm^3/g) prepared via the postsynthetic ligand exchange (Supporting Information Table S5). During the soaking of GP-d in bipy solution, not only the pillar exchange from pz to bipy to produce GB-e but also the localized elimination of some [Ni(HBTC)(pz)] fragments in the 2-D sheets have simultaneously occurred to lead to the framework of the larger pore volume while retaining the overall framework integrity. The N_2 adsorption amounts on HB-d and GB-e (or GB-i) are also negligible at 298 K, as on GP-d and HP-e.

Pore Size Distributions of the Activated MOFs. The pore size distribution of GP-d calculated using the SF model is similar to that of HP-e (Supporting Information Figure S11).[19] Even though the total pore volume of HP-e is slightly larger than that of GP-d, the average pore dimension of HP-e (9.1 Å) is smaller than that of GP-d (9.3 Å). The BET and the Langmuir surface areas of HP-e calculated from the N_2 adsorption isotherm are also slightly larger than those of GP-d (Table 1 and Supporting Information Figures S12 and S13). The N_2 adsorption isotherms of HB-d and GB-e (or GB-i) show that the pore volumes of HB-d and GB-e (or GB-i) with the longer bipy pillar are larger than those of HP-e and GP-d with the shorter pz pillar.

CO_2 Adsorptions. CO_2 adsorption behaviors on HB-d, GB-e, GB-i, HP-e, and GP-d at 195 K are expected from the single-crystal structures of the MOFs (Supporting Information Figure S14). The CO_2 uptake amounts are related to the pore volumes of the MOFs, which depend on the lengths of the pillaring linkers, bipy and pz. HB-d and GB-e (or GB-i) with the longer bipy pillar show the larger uptake amounts of CO_2 at 1 bar than those of HP-e and GP-d with the shorter pz pillar.

The CO_2 adsorption behaviors at 273 and 298 K are different from those at 195 K (Figure 11 and Supporting Information

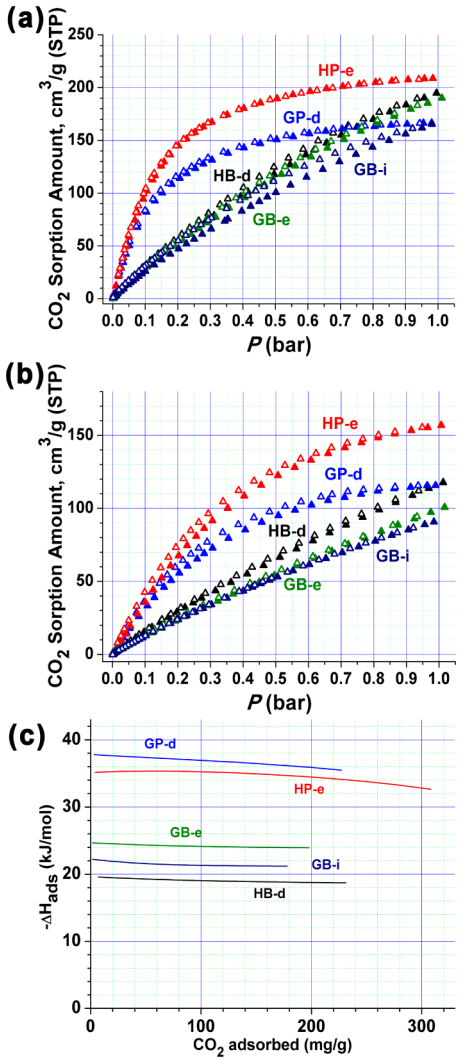

Figure 11. CO_2 sorption isotherms on HB-d, GB-e, GB-i, HP-e, and GP-d at (a) 273 K and (a) 298 K and (c) their adsorption enthalpies.

Figure S15; Table 2 and Supporting Information Table S5). HP-e with pz as a pillar shows the largest uptakes at both ~0.15 bar (the approximate CO_2 partial pressure of flue gas) and 1 bar. The CO_2 sorption behavior on GP-d with the same pz pillar is similar to that on HP-e, but the adsorption amounts at both ~0.15 and 1 bar are smaller than the corresponding amounts on HP-e. The CO_2 sorption behaviors of HB-d and GB-e (or GB-i) with bipy pillar at 273 and 298 K are quite different from those of HP-e and GP-d with a pz pillar. While the CO_2 uptakes on HB-d and GB-e (or GB-i) at ~0.15 bar are significantly smaller than those on GP-d and HP-e, the uptakes at ~1 bar are comparable to those on GP-d and HP-e. The

dx.doi.org/10.1021/cm404239s | *Chem. Mater.* 2014, 26, 1711−1719

Table 2. PSA and VSA CO_2 Working Capacities of MOFs

MOFs	BET surface area (m^2 g^{-1})	PSA (mmol g^{-1})	VSA (mmol g^{-1})	Qst (kJ mol^{-1})	reference
HB-d	1940	4.7 (4.3)[a]	1.8	19.6	this work
HP-e	1210	4.6 (4.7)[a]	3.9	35.2	this work
GP-d	1090	3.3 (3.2)[a]	3.0	37.8	this work
GB-e	1840	4.0 (3.7)[a]	1.5	24.7	this work
GB-i	1790	– (3.3)[a]	1.4	22.2	this work
HKUST-1	1690	4.5	1.6	26	7
PCN-11	1931	4.0	1.4	23	7
PCN-16	2273	3.3	1.1	23	7
Zn-MOF-74	885	3.6	2.7	30	7
Mg-MOF-74	1332	2.1	4.1	45	7
MOF-5	3500	0.7	0.2	15	7
ZIF-8	1980	0.7	0.2	17	7

[a]The PSA working CO_2 capture capacities were calculated as the differences of the CO_2 adsorption amounts at 1.2 and 0.2 bar, and the PSA working CO_2 capture capacities in parentheses are the values calculated as the differences of the CO_2 adsorption amounts at 1.0 and 0.15 bar.

frameworks of HB-d and GB-e (or GB-i) with the larger pore dimensions have smaller CO_2 adsorption enthalpies than those of HP-e and GP-d. The smaller CO_2 adsorption enthalpies of HB-d and GB-e (or GB-i) than those of HP-e and GP-d led to the smaller CO_2 uptakes at ~0.15 bar and the larger pore volumes of HB-d and GB-e (or GB-i) than those of HP-e and GP-d, and the appropriate CO_2 adsorption enthalpies resulted in comparable CO_2 uptakes at ~1 bar.

Working CO_2 Capture Capacity. The CO_2 uptake amount of HP-e at 298 K and ~1 bar (23.6% (157 cm^3/g)) is slightly smaller than that of the best MOF, Mg-MOF-74 (27.4%), in the same condition.[20] However, the working CO_2 capture capacity, defined as the difference in adsorbed amounts between two specific conditions, two different temperatures for the TSA process and two different pressures for the VSA and PSA processes, is more important for the true CO_2 capture performance. Even for the same MOF, the working CO_2 capture capacity is dependent on the type of the capture processes employed. For the VSA process, the presence of a strong adsorption site is essential for large working CO_2 capture capacity because of the low partial pressure of CO_2 in the flue gas.[8] Mg-MOF-74 with strongly interacting open metal sites showed the largest CO_2 uptake in the low-pressure region,[20] and the VSA working CO_2 capture capacity (between 0.3 and 0.01 bar) is 4.1 mmol/g, which is the largest reported (Table 2).[4] Although HP-e does not have any open metal sites, its CO_2 adsorption enthalpy is quite high (35.2 kJ/mol), and the VSA working CO_2 capture capacity is 3.9 mmol/g, which is only slightly lower than the largest capture capacity of Mg-MOF-74. For the PSA process between the pressurized real flue gas of ~6 bar and the depressurized gas of ~1 bar, a moderate adsorption enthalpy of MOFs with tuned pore geometries and surface properties is more important in determining the working CO_2 capture capacity than the large adsorption enthalpy.[7] Because the CO_2 partial pressures of the pressurized and depressurized real flue gas correspond to 1.0−1.2 bar and 0.15−0.2 bar, respectively, the working CO_2 capture capacity of an MOF in the PSA process corresponds to the difference in the adsorbed amounts between 1.0−1.2 bar and 0.15−0.2 bar of pure CO_2 gas. The PSA working CO_2 capture capacity of HP-e (between 1.2 and 0.2 bar) is 4.6 mmol/g (Figure 11 and Supporting Information Figure S15; Table 2 and Supporting Information Table S5), which is even slightly larger than the largest PSA capture capacity of HKUST-1, 4.5 mmol/g, at the same condition. The PSA working CO_2 capture capacity of HP-e between 1.0 to 0.15 bar (4.7 mmol/g) is even slightly larger than the PSA capture capacity of the same HP-e between 1.2 to 0.2 bar (4.6 mmol/g). The capture performance of an MOF can be varied depending on the specific process conditions. The working CO_2 capture capacity of an MOF varies slightly depending on the exact adsorption and desorption conditions chosen. The VSA working CO_2 capture capacity of HB-d with the larger pore volume and BET surface area than those of HP-e is only 1.8 mmol/g. The small VSA working CO_2 capture capacity is related to the small adsorption enthalpy of HB-d. However, the PSA working CO_2 capture capacity of HB-d between 1.2 to 0.2 bar is the largest, 4.7 mmol/g. Even though the adsorption enthalpy of HP-e is slightly smaller than that of GP-d, the PSA working CO_2 capture capacity of HP-e is much larger than that of GP-d. The surface area also affects the PSA capture capacity. The larger PSA working CO_2 capture capacity of HP-e than that of GP-d might be due to the larger surface area of HP-e.

■ CONCLUSIONS

A series of isoreticular and polymorphic 3-D MOFs could be prepared via the combination of (a) direct solvothermal reaction using Ni(II) ion and H_3BTC as building components for the 2-D sheet of an **hcb** topology and bipy or pz as a pillar between the sheets and (b) PLE of, and PLI into, the MOF prepared via the direct solvothermal reaction. The microporous 3-D MOF, HB-d, of a 3,5-c **hms** topology could be prepared via a one-pot solvothermal reaction. However, a similar solvothermal reaction in the presence of pz only produced another microporous 3-D MOF, GP-d, of the same 3,5-connection but different net topology, **gra** topology. HP-e could only be obtained via the PLE. Similarly, GB-e or GB-i, which is isoreticular to GP-d, could be obtained via either the PLE or the PLI. The series of isoreticular and/or polymorphic MOFs are microporous and show interesting CO_2 sorption behaviors. Although the BET surface areas of the MOFs are not so large, the MOFs do not contain any open metal sites, and the adsorption enthalpies are not very high, the PSA working CO_2 capture capacities of HB-d and HP-e are the largest among the reported MOFs. The appropriate pore dimension, surface area, and adsorption enthalpy could work better for the larger working CO_2 capture capacity via the PSA process. The balance between the high adsorption enthalpy and the large surface area might be important for the high PSA CO_2 capture capacity. This work demonstrates the utility of the combinational

synthetic approaches for the tuning of the pore geometry with desired surface property.

■ ASSOCIATED CONTENT

Supporting Information

CIF files and crystal structure analyses; tables of crystal data and structure refinement; a table of the CO_2 sorption behaviors; PXRD patterns of HP-e; optical photographs of the activated crystals; figures of the cage-like pores; NMR spectra, TGA data, and PXRD patterns of the activated samples; pore size distributions and BET and Langmuir surface areas of the activated samples; CO_2 sorption isotherms at 195 K; and CO_2 sorption isotherms up to ∼1.2 bar at 298 K. This material is available free of charge via the Internet at http://pubs.acs.org.

■ AUTHOR INFORMATION

Corresponding Author

*E-mail: mslah@unist.ac.kr.

Notes

The authors declare no competing financial interest.

■ ACKNOWLEDGMENTS

This work was supported by NRF-2010-0019408 and NRF-2012R1A2A2A01003077 through the National Research Foundation of Korea. The authors acknowledge PAL for beam line use (2013-first-2D-007).

■ ABBREVIATIONS

BET, Brunauer−Emmett−Teller; bipy, 4,4′-bipyridine; DMF, *N*,*N*′-dimethylformamide; EA, elemental analysis; H_3BTC, 1,3,5-benzenetricarboxylic acid; MOF, metal−organic framework; PLE, postsynthetic ligand exchange; PLI, postsynthetic ligand insertion; PSA, pressure swing adsorption; PXRD, powder X-ray diffraction; pz, pyrazine; TGA, thermal gravimetric analysis; TSA, temperature swing adsorption; VSA, vacuum swing adsorption

■ REFERENCES

(1) (a) Furukawa, H.; Cordova, K. E.; O'Keeffe, M.; Yaghi, O. M. *Science* **2013**, *341*, 973−987. (b) Zhou, H. C.; Long, J. R.; Yaghi, O. M. *Chem. Rev.* **2012**, *112*, 673−674.

(2) (a) Suh, M. P.; Park, H. J.; Prasad, T. K.; Lim, D. W. *Chem. Rev.* **2012**, *112*, 782−835. (b) Zhou, W. *Chem. Rec.* **2010**, *10*, 200−204. (c) Li, J. R.; Sculley, J.; Zhou, H. C. *Chem. Rev.* **2012**, *112*, 869−932. (d) Yoon, M.; Srirambalaji, R.; Kim, K. *Chem. Rev.* **2012**, *112*, 1196−1231.

(3) (a) Cohen, S. M. *Chem. Rev.* **2011**, *112*, 970−1000. (b) Allen, C. A.; Cohen, S. M. *J. Mater. Chem.* **2012**, *22*, 10188−10194. (c) Tuci, G.; Rossin, A.; Xu, X.; Ranocchiari, M.; van Bokhoven, J. A.; Luconi, L.; Manet, I.; Melucci, M.; Giambastiani, G. *Chem. Mater.* **2013**, *25*, 2297−2308. (d) Hindelang, K.; Kronast, A.; Vagin, S. I.; Rieger, B. *Chem. − Eur. J* **2013**, *19*, 8244−8252. (e) Sun, F.; Yin, Z.; Wang, Q.-Q.; Sun, D.; Zeng, M.-H.; Kurmoo, M. *Angew. Chem., Int. Ed.* **2013**, *52*, 4538−4543. (f) Bloch, W. M.; Babarao, R.; Hill, M. R.; Doonan, C. J.; Sumby, C. J. *J. Am. Chem. Soc.* **2013**, *135*, 10441−10448.

(4) (a) Lalonde, M.; Bury, W.; Karagiaridi, O.; Brown, Z.; Hupp, J. T.; Farha, O. K. *J. Mater. Chem. A* **2013**, *1*, 5453−5468. (b) Dincă, M.; Long, J. R. *J. Am. Chem. Soc.* **2007**, *129*, 11172−11176. (c) Das, S.; Kim, H.; Kim, K. *J. Am. Chem. Soc.* **2009**, *131*, 3814−3815. (d) Mukherjee, G.; Biradha, K. *Chem. Commun.* **2012**, *48*, 4293−4295. (e) Song, X.; Kim, T. K.; Kim, H.; Kim, D.; Jeong, S.; Moon, H. R.; Lah, M. S. *Chem. Mater.* **2012**, *24*, 3065−3073. (f) Song, X.; Jeong, S.; Kim, D.; Lah, M. S. *CrystEngComm* **2012**, *14*, 5753−5756. (g) Zhang, Z.; Wojtas, L.; Eddaoudi, M.; Zaworotko, M. J. *J. Am. Chem. Soc.* **2013**, *135*, 5982−5985. (h) Kim, Y.; Das, S.; Bhattacharya, S.; Hong, S.; Kim, M. G.; Yoon, M.; Natarajan, S.; Kim, K. *Chem. − Eur. J.* **2012**, *18*, 16642−16648. (i) Wei, Z.; Lu, W.; Jiang, H.-L.; Zhou, H.-C. *Inorg. Chem.* **2013**, *52*, 1164−1166.

(5) (a) Burnett, B. J.; Barron, P. M.; Hu, C.; Choe, W. *J. Am. Chem. Soc.* **2011**, *133*, 9984−9987. (b) Burnett, B. J.; Choe, W. *Dalton Trans.* **2012**, *41*, 3889−3894. (c) Kim, M.; Cahill, J. F.; Su, Y.; Prather, K. A.; Cohen, S. M. *Chem. Sci.* **2012**, *3*, 126−130. (d) Bury, W.; Fairen-Jimenez, D.; Lalonde, M. B.; Snurr, R. Q.; Farha, O. K.; Hupp, J. T. *Chem. Mater.* **2013**, *25*, 739−744. (e) Burnett, B. J.; Choe, W. *CrystEngComm* **2012**, *14*, 6129−6131. (f) Karagiaridi, O.; Bury, W.; Sarjeant, A. A.; Stern, C. L.; Farha, O. K.; Hupp, J. T. *Chem. Sci.* **2012**, *3*, 3256−3260. (g) Takaishi, S.; DeMarco, E. J.; Pellin, M. J.; Farha, O. K.; Hupp, J. T. *Chem. Sci.* **2013**, *4*, 1509−1513. (h) Jeong, S.; Kim, D.; Song, X.; Choi, M.; Park, N.; Lah, M. S. *Chem. Mater.* **2013**, *25*, 1047−1054. (i) Kim, M.; Cahill, J. F.; Fei, H.; Prather, K. A.; Cohen, S. M. *J. Am. Chem. Soc.* **2012**, *134*, 18082−18088. (j) Li, T.; Kozlowski, M. T.; Doud, E. A.; Blakely, M. N.; Rosi, N. L. *J. Am. Chem. Soc.* **2013**, *135*, 11688−11691. (k) Gross, A. F.; Sherman, E.; Mahoney, S. L.; Vajo, J. J. *J. Phys. Chem. A* **2013**, *117*, 3771−3776.

(6) (a) Sumida, K.; Rogow, D. L.; Mason, J. A.; McDonald, T. M.; Bloch, E. D.; Herm, Z. R.; Bae, T. H.; Long, J. R. *Chem. Rev.* **2012**, *112*, 724−781. (b) Furukawa, H.; Ko, N.; Go, Y. B.; Aratani, N.; Choi, S. B.; Choi, E.; Yazaydin, A. O.; Snurr, R. Q.; O'Keeffe, M.; Kim, J.; Yaghi, O. M. *Science* **2010**, *329*, 424−428. (c) Farha, O. K.; Yazaydın, A. O.; Eryazici, I.; Malliakas, C. D.; Hauser, B. G.; Nguyen, M. G. K. S. T.; Snurr, R. Q.; Hupp, J. T. *Nat. Chem.* **2010**, *2*, 944−948. (d) Grünker, R.; Bon, V.; Heerwig, A.; Klein, N.; Müller, P.; Stoeck, U.; Baburin, I. A.; Mueller, U.; Senkovska, I.; Kaskel, S. *Chem. − Eur. J.* **2012**, *18*, 13299−13303. (e) Millward, A. R.; Yaghi, O. M. *J. Am. Chem. Soc.* **2005**, *127*, 17998−17999. (f) Song, X.; Oh, M.; Lah, M. S. *Inorg. Chem.* **2013**, *52*, 10869−10876.

(7) Simmons, J. M.; Wu, H.; Zhou, W.; Yildirim, T. *Energy Environ. Sci.* **2011**, *4*, 2177−2185.

(8) (a) Mason, J. A.; Sumida, K.; Herm, Z. R.; Krishna, R.; Long, J. R. *Energy Environ. Sci.* **2011**, *4*, 3030−3040. (b) Cho, M. T.; Allinson, G. W.; Wiley, D. E. *Ind. Eng. Chem. Res.* **2008**, *47*, 4883−4890. (c) Na, B. K.; Koo, K. K.; Eum, H. M.; Lee, H.; Song, H. K. *Kor. J. Chem. Eng.* **2001**, *18*, 220−227.

(9) (a) Herm, Z. R.; Swisher, J. A.; Smit, B.; Krishna, R.; Long, J. R. *J. Am. Chem. Soc.* **2011**, *133*, 5664−5667. (b) Caskey, S. R.; Wong-Foy, A. G.; Matzger, A. J. *J. Am. Chem. Soc.* **2008**, *130*, 10870−10871. (c) Dietzel, P. D. C.; Johnsen, R. E.; Fjellvag, H.; Bordiga, S.; Groppo, E.; Chavan, S.; Blom, R. *Chem. Commun.* **2008**, 5125−5127. (d) Britt, D.; Furukawa, H.; Wang, B.; Glover, T. G.; Yaghi, O. M. *Proc. Nat. Acad. Sci. U.S.A.* **2009**, *106*, 20637−20640. (e) Yazaydın, A. Ö.; Benin, A. I.; Faheem, S. A.; Jakubczak, P.; Low, J. J.; Willis, R. R.; Snurr, R. Q. *Chem. Mater.* **2009**, *21*, 1425−1430. (f) Nugent, P.; Belmabkhout, Y.; Burd, S. D.; Cairns, A. J.; Luebke, R.; Forrest, K.; Pham, T.; Ma, S.; Space, B.; Wojtas, L.; Eddaoudi, M.; Zaworotko, M. J. *Nature* **2013**, *495*, 80−84. (g) Xiang, S.; He, Y.; Zhang, Z.; Wu, H.; Zhou, W.; Krishna, R.; Chen, B. *Nat. Commun.* **2012**, *3*, 954. (h) Dzubak, A. L.; Lin, L.-C.; Kim, J.; Swisher, J. A.; Poloni, R.; Maximoff, S. N.; Smit, B.; Gagliardi, L. *Nat. Chem.* **2012**, *4*, 810−816.

(10) (a) Arstad, B.; Fjellvåg, H.; Kongshaug, K.; Swang, O.; Blom, R. *Adsorption* **2008**, *14*, 755−762. (b) Couck, S.; Denayer, J. F. M.; Baron, G. V.; Rémy, T.; Gascon, J.; Kapteijn, F. *J. Am. Chem. Soc.* **2009**, *131*, 6326−6327. (c) Demessence, A.; D'Alessandro, D. M.; Foo, M. L.; Long, J. R. *J. Am. Chem. Soc.* **2009**, *131*, 8784−8786. (d) Vaidhyanathan, R.; Iremonger, S. S.; Dawson, K. W.; Shimizu, G. K. H. *Chem. Commun.* **2009**, 5230−5232. (e) An, J.; Geib, S. J.; Rosi, N. L. *J. Am. Chem. Soc.* **2009**, *132*, 38−39. (f) Vaidhyanathan, R.; Iremonger, S. S.; Shimizu, G. K. H.; Boyd, P. G.; Alavi, S.; Woo, T. K. *Science* **2010**, *330*, 650−653. (g) Zheng, B.; Bai, J.; Duan, J.; Wojtas, L.; Zaworotko, M. J. *J. Am. Chem. Soc.* **2010**, *133*, 748−751. (h) Duan, J.; Yang, Z.; Bai, J.; Zheng, B.; Li, Y.; Li, S. *Chem. Commun.* **2012**, *48*, 3058−3060. (i) Planas, N.; Dzubak, A. L.; Poloni, R.; Lin, L.-C.;

McManus, A.; McDonald, T. M.; Neaton, J. B.; Long, J. R.; Smit, B.; Gagliardi, L. *J. Am. Chem. Soc.* **2013**, *135*, 7402−7405.
(11) *Materials Studio program*, version 4.3; Accelrys: San Diego, CA, 2008.
(12) Here and in ref 13, the 2-D sheet structure in the 3-D MOFs is formulated as [Ni(HBTC)]. However, the correct formulation is $[Ni_3(BTC)(HBTC)(H_2BTC)]$ because the H_3BTC ligands in the 2-D sheet are in three different deprotonated states. One is in the form of a fully deprotonated BTC^{3-} state with all carboxylate groups in a chelating bidentate binding mode, and the others are in the form of partially deprotonated $H_2BTC^{1-}/HBTC^{2-}$ states with all carboxylate groups in a monodentate binding mode. The ligands in the partially deprotonated $H_2BTC^{1-}/HBTC^{2-}$ states are involved in interligand hydrogen bonding in the 2-D sheet of an **hcb** (honeycomb) topology.
(13) Gao, C.; Liu, S.; Xie, L.; Ren, Y.; Cao, J.; Sun, C. *CrystEngComm* **2007**, *9*, 545−547.
(14) Gao, C.; Liu, S.; Xie, L.; Sun, C.; Cao, J.; Ren, Y.; Feng, D.; Su, Z. *CrystEngComm* **2009**, *11*, 177−182.
(15) Unfortunately, the quality of the HP-d crystals obtained via the reported procedure was not good enough for single-crystal structure analysis.
(16) The polymorphic MOFs of 3,5-c **hms** and **gra** topologies are of the same long vertex symbol, $(6_3{\cdot}6_3{\cdot}6_3)(6{\cdot}6{\cdot}6{\cdot}6_2{\cdot}6_2{\cdot}6_2{\cdot}6_2{\cdot}6_2{\cdot}6_2{\cdot}*)$, but have different connectivities between 2-D sheets of an **hcb** topology with eclipsed and staggered arrangements, respectively. Please see the web site http://rcsr.anu.edu.au/rcsr_nets/search.
(17) While the three different protonated forms of the ligands in GP-d, $BTC^{3-}/HBTC^{2-}/H_2BTC^{-}$, are statistically disordered in the hexagonal $P6_3/mmc$ space group, all of the ligands in GP-i belonging to the lower symmetry monoclinic *Cc* space group are structurally well resolved in the BTC^{3-} and two $HBTC^{2-}/H_2BTC^{-}$ forms (Figure 7).
(18) The N_2 uptake amount of the activated HB-d is significantly larger than that of the reported HB-d (391 cm^3/g), which was prepared by soaking the crystals of the as-synthesized HB-d in fresh DMF for 2−3 d and by vacuum-drying at 150 °C overnight.[5h] The different activation process significantly affects the porosity of HB-d.
(19) Saito, A.; Foley, H. C. *AIChE J.* **1991**, *37*, 429−436.
(20) McDonald, T. M.; D'Alessandro, D. M.; Krishna, R.; Long, J. R. *Chem. Sci.* **2011**, *2*, 2022−2028.